

Terahertz hyperspectral imaging with dual chip-scale combs: supplementary material

LUKASZ A. STERCZEWSKI^{1,2,†}, JONAS WESTBERG^{1,†}, YANG YANG³, DAVID BURGHOFF^{3,4}, JOHN RENO⁵, QING HU^{3,*}, AND GERARD WYSOCKI^{1,**}

¹Department of Electrical Engineering, Princeton University, Princeton, New Jersey 08544, USA

²Faculty of Electronics, Wrocław University of Science and Technology, Wrocław 50370, Poland

³Department of Electrical Engineering and Computer Science, Research Laboratory of Electronics, Massachusetts Institute of Technology, Cambridge, MA 02139, USA

⁴Department of Electrical Engineering, University of Notre Dame, Notre Dame, IN 46556, USA

⁵Center for Integrated Nanotechnology, Sandia National Laboratories, Albuquerque, NM 87123, USA

[†]These authors contributed equally to this work.

*Corresponding author: qhu@mit.edu

**Corresponding author: gwyssocki@princeton.edu

Published 31 May 2019

This document provides supplementary information to "Terahertz hyperspectral imaging with dual chip-scale combs," <https://doi.org/10.1364/OPTICA.6.000766>.

1. LASER FABRICATION

Laser fabrication follows the standard process for metal-metal waveguide THz QCLs. Both lasers are roughly 2 mm in length, resulting in repetition around 17 GHz, which was intentionally doubled compared to our previous works [1, 2] to provide more power per mode within a given comb bandwidth. This provides better compatibility with solid state THz spectroscopy, where the linewidths of crystal lattice vibrations reach tens of gigahertz. The widths of the lasers are 20 μm to ensure single transverse mode operation. To compensate for the dispersion, we have made use of a double-chirped sinusoidal structure with optimized parameters based on measured dispersion data [1]. The period of the sinusoidal corrugation is linearly chirped from 8.5 μm to 15.75 μm , and the amplitude of the corrugation is chirped in the same fashion. As a result, a 336 μm long dispersion compensator section introduces a 2nd order dispersion of 0.5568 ps², which cancels the measured dispersion in the range of 3–4 THz. The devices were butt-coupled to a 4 mm diameter high-resistivity float zone silicon (HRFZ-Si) hyperhemispherical lens with a 500 μm thick HRFZ-Si spacer in between. The lens pre-collimates the THz light for efficient collection with external optics outside the cryostat wherein the devices are operated, albeit with a slight broadening of the intermode beat note due to an increased amount of optical feedback caused by residual Fresnel reflections from the lens interface.

2. OPERATION OF THE THZ-QCLS

The two lensed THz QCL combs were soldered to copper heat sinks and housed in a vacuum-insulated, vibration-dampened Gifford-McMahon (GM) pulsed tube cryostat (Coldedge) with a cold finger temperature of 25 K under laser bias conditions. To facilitate electrical extraction of the microwave intermode beat note, the lasers were biased through a cryogenic stainless steel shielded coaxial cable (CryoCoax) coiled around the first stage of the cryocooler, which accounts for the additional heat load due to a thermal link with ambient. Outside the cryostat, the coax is terminated with a 40 GHz bias tee (SigaTek SB15D2) separating the microwave signal from a DC bias provided by low noise QCL drivers (Wavelength Electronics, QCL-2000+) supplied from an insulated linear power supply. When biased in the comb regime at ~ 350 mA, and 11.70 V, the QCL chips emit an array of discrete and uniformly spaced THz lines with high degree of mutual coherence [1], which gives rise to a strong microwave signal appearing at the roundtrip frequency of the lasers caused by nonlinear electrical characteristics of the lasing medium. These intermode beat note signals were measured simultaneously from both lasers after combining the RF ports of the microwave bias tees using a sensitive real-time spectrum analyzer (F&S RSW-43) within an acquisition time of 10 ms. The discrepancy in the measured 3 dB linewidths of 18 kHz and 57 kHz [Fig. 1(e) and (f) of the main manuscript] is mainly due to a higher susceptibility of the broader-linewidth laser to mechanical vibrations induced by the cryocooler. Since the linewidth of the down-converted RF

spectrum scales approximately with the optical mode number N (see Ref. [3]), at 3.4 THz $N = 200$ translates into a theoretical multiheterodyne beat note line width of ~ 10 MHz, which agrees well with that retrieved from the spectrum shown in Fig. 2(a) in the main manuscript. It should be emphasized, however, that the system was completely free-running, and in principle further reduction in line width can be obtained through an active stabilization of the lasers as in Ref. [4], together with more effective dampening of cryostat vibrations.

3. OPTICAL POWER MEASUREMENT

The amount of power emitted by each device was measured with a calibrated photo-acoustic THz optical power meter (Absolute Terahertz Power/Energy Meter, TK Instruments) after absorption and Fresnel losses introduced by the lenses, and the cryostat's polymethylpentene (PMP/ TPXTM) output windows. The estimated optical output power $>100 \mu\text{W}$ from each device is enough to suppress superconductivity of our niobium nitride (NbN) hot-electron bolometer (Scontel, RS-LH2L-0.3-4T-0.05/1/10000), therefore the light was attenuated with irises placed before the beam splitter to ensure operation of the bolometer in the linear regime.

4. FOURIER TRANSFORM SPECTROMETER CHARACTERIZATION

The optical spectra of the THz-QCL OFCs were characterized with a home-made Fourier Transform spectrometer (FTS) utilizing a Ga doped Ge photodetector whose input port was periodically modulated by an optical chopper rotating at 100 Hz. Samples in the interferogram were acquired synchronously with a He-Ne laser-based fringe trigger and acquired with a lock-in amplifier. Next the acquired data [Fig. 1(d) of the main manuscript] were converted into a power spectrum through a Fast Fourier Transform, as plotted in Fig. (1)c. The resolution of the measurement was 0.4 cm^{-1} , limited by the FTS maximum optical path difference (OPD).

5. IMAGING OPTICS

A schematic of the imaging system is included in the main document [Fig. 1(a)], and here a more detailed description is given. For convenience, we show a 2D version of the experimental schematic in Fig. S1. Light from the lensed THz-QCL OFCs arranged in anti-parallel configuration were collected from opposite sides of the cryostat using two 2-inch off-axis parabolic mirrors (OAPMs) with an effective focal length (EFL) of 4 inches (~ 10 cm). Next, the collimated THz beam from the signal (Sig.) laser was focused on the sample using a similar OAPM with an EFL of 2 inches (~ 5 cm), and re-collimated after propagating through the sample. Finally, the signal and the local oscillator (LO) beams were combined on a HRFZ-Si beam splitter and guided to the hot electron bolometer. All mirrors in the system were 2 inches (~ 5 cm) in diameter and used gold as a reflective surface.

6. MULTIHETERODYNE DOWNCONVERSION

To optically multiheterodyne the dual-comb light, we coupled it into the bolometer using a 2-inch (~ 5 cm) gold OAPM with an EFL of 6 inches (~ 15 cm). The difference in repetition rates Δf_{rep} and offset frequencies Δf_0 gives rise to an optical mixing microwave photocurrent signal centered in frequency around

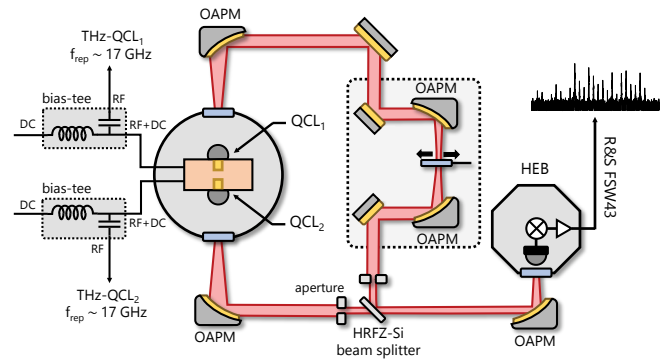


Fig. S1. 2D experimental schematic of the THz hyperspectral imaging system. The two THz-QCL OFCs are housed in a cryo-cooler at 25 K and aligned in an anti-parallel fashion. One of the laser beams (probe beam) is focused onto the solid sample placed on a raster-scanning translation stage. After propagation through the sample, the probe is re-collimated and overlapped with the other laser beam on a HRFZ-Si beam splitter. The combined beams are heterodyned on a liquid helium-cooled hot electron bolometer whose output is digitized with a 43 GHz spectrum analyzer.

Δf_0 and periodic in time with a period of $1/\Delta f_{\text{rep}}$. The rf signal was amplified by an HEMT cryogenic amplifier in the bolometer. The radio frequency spectrum of the beating interferogram was recorded with a spectrum analyzer and further processed numerically (see Processing of the hyperspectral image). Throughout the duration of the experiment, the measurement chamber was continuously purged with dry nitrogen to minimize the influence of water vapor absorption.

7. PROCESSING OF THE HYPERSPECTRAL IMAGE

Raw dual-comb THz spectra were recorded at different positions of the raster-scanning mechanical stage using a spectrum analyzer connected to the superconducting hot electron bolometer. Each rf spectrum was converted into an array of peak beat note powers assigned to each pixel, with a threshold criterion to select only beat notes of sufficiently high contrast. This resulted in an 81×53 pixel hyperspectral image cube with 12 frequency bands. To obtain transmission images, T_ν , the intensity of the hyperspectral image in each frequency band (hyperspectral slice) was normalized to the mean intensity of a fully transparent part of the image (upper left corner). This was further converted into a more suitable log-scale for analysis of solid samples. Finally, to suppress the measurement noise and sample scattering effects, each hyperspectral slice was smoothed with a Gaussian filter. The three slices displayed in Fig. S2(a) are located in the optical domain at $\nu_R = 3.30$ THz, $\nu_G = 3.35$ THz, and $\nu_B = 3.45$ THz, and constitute the false red (R), green (G) and blue (B) color channels in the RGB composite transmission image shown in the main manuscript (Fig. 4). However, here the data is shown without any equalization of pixel intensities.

Because the diluting polyethylene matrix (HDPE) introduces a non-negligible absorption and scattering losses above 3 THz, it dominates in the image and inevitably causes a decrease in contrast. Consequently, weaker changes caused by the frequency-dependent absorption in the different zones of the imaged pellet are less pronounced. A remedy to this issue is to equalize (flatten) the histograms of the images to increase their dynamic

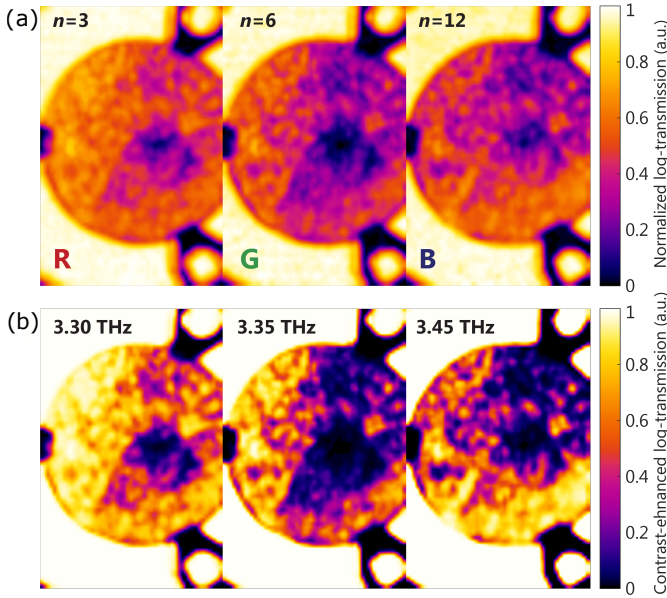


Fig. S2. Raw and contrast-enhanced THz composite image channels. (a) Normalized log-transmission images of the false R, G, and B color channel extracted from the 3rd, 6th, and 12th beat note of the frequency spectrum located at 3.30 THz, 3.35 THz, and 3.45 THz, respectively. (b) Contrast-enhanced image of (a). Bright intensity corresponds intuitively to high transparency in the THz.

range, and hence enhance the contrast of the features of interest. The histograms of the raw absorbance images of Fig. S2(a) are shown in Fig. S3(b) and reveal a Gaussian-like shape centered around ~ 0.45 . This stems from the fact that a considerable number of pixels falls into a narrow intensity range. We apply a sigmoidal transformation, also known as the logistic curve, to globally adjust the hyperspectral image intensities and thereby spread their intensities more evenly:

$$I_C(I) = \frac{1}{1 + e^{-k(I-I_0)}}, \quad (\text{S1})$$

where I_C denotes the intensity of a corrected pixel, k is the steepness of the curve, and I_0 is the abscissa of the curve's midpoint. The results of this operation [with the used correction profiles displayed in Fig. S2(a)] are clearly visible in Fig. S2(b), where each channel shows a rapid transition between the weakly absorbing zone of L-histidine hydrochloride monohydrate, and the more absorbing α -D-glucose and α -D-lactose monohydrates. Also, the histograms of the equalized image shown in Fig. S3(c) have been flattened in the central part, while leaving the background and non-transparent parts saturated.

Since Fig. S2(b) shows the optical transmission, it is expected that the left zone of the pellet with high transparency in all the composite channels will be almost white in the final false-color image, whereas the top right zone with almost no transmission in the G and B channels should appear as red. The bottom zone on the contrary shows high transmission predominantly in the blue channel with moderate attenuation in the red, hence it appears as purple in Fig. S4. The origin of this behavior can be explained by analyzing the spectroscopic data plotted in Fig. 4(b) in the main manuscript. The α -D-glucose monohydrate zone transmits THz light effectively only in the red channel at 3.30 THz THz, whereas the α -D-lactose zone is the most trans-

parent in the blue channel at 3.45 THz. The last L-histidine hydrochloride monohydrate zone shows the highest transparency of all with a slightly pronounced absorption in the blue region, hence it appears as orange-white. Here, it should be mentioned that no special color maps or sophisticated feature extraction techniques were used to obtain this image, which is merely a superposition of the false-color monochromatic slices of Fig. S2(b). In other words, a sample with the same absorption profiles at visible wavelengths as those shown here in the THz, would look nearly the same in transmission when illuminated by a visible white light source. Without the hyperspectral character of the image data, the slope-dependent discrimination between the different absorbers, visible as regions with distinct colors in the THz composite image, would not have been possible.

To better visualize the frequency-dependent character of the sample, Fig. 4(a) in the main document shows absorbance images ($A_v = \log_{10}(T_v)$) after band-wise mean-normalization to enhance the slice-to-slice variation in absorption, followed by the same contrast enhancement procedure as discussed earlier. Red zones in the R, G, and B slices correspond to absorbance stronger than the average, whereas the blue indicate less absorption.

8. IMAGING OF PHARMACEUTICALS IN NATIVE PACKAGING

To evaluate the feasibility of non-invasive imaging of marketed pharmaceuticals in native packaging, we extended the transmission measurements with reflection, where the focusing and re-collimating OAPMs were aligned to guide the beam to the sample and collect the light reflected its surfaces. The incidence angle to the sample was approximately 30° . Just as in the transmission measurements, the sample raster scanned to obtain the image. As a test sample, we used a marketed antihistamine drug used to treat allergies (Benadryl[®]) in a blister pack, which is one of the most-widespread types of pharmaceutical packaging. The top layer of the packaging is made of an optically transparent polymer (which is transparent in the THz as well), whereas the backing acts as a lidding seal made of aluminum foil, thus forming a protected cavity for the tablet. The metal layer precludes transmission measurements, yet enables to take advantage of the efficient THz reflection from the metallic interface as well

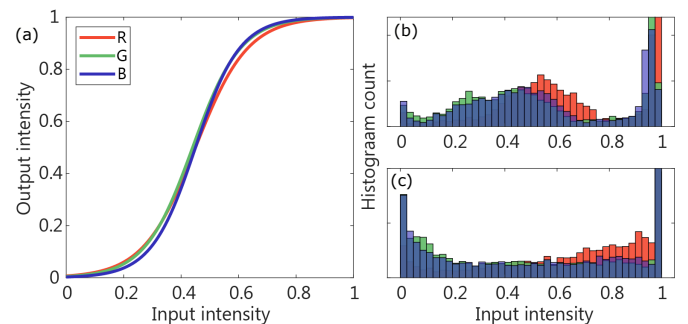


Fig. S3. Histogram equalization for contrast enhancement. (a) RGB correction curves used in the equalization procedure. (b) Histogram of pixel intensities in the raw log-transmission data from Fig. S2(a) for the individual composite channels. (c) Histogram of the contrast-enhanced data from Fig. S2(b). The last bin corresponds to the intentionally saturated white background.

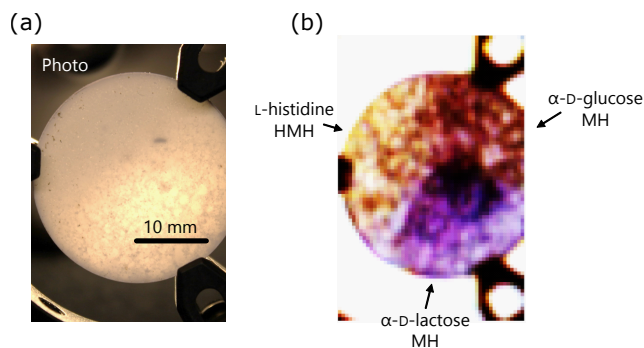


Fig. S4. Comparison of the visible and hyperspectral image. (a) Backlit visible light photo of the pressed sample disc in the metal sample holder. (b) THz hyperspectral image obtained from the composite false RGB color channels shown in Fig. S2(b). The slight variation in intensity, as well as the presence of darker regions in the sample is caused mainly by the inhomogeneity of the absorbers within the hosting polyethylene matrix. While the raw powdered samples were ground with a pestle and mortar into fine particles prior to thorough mixing following the procedures in Ref. [5], local clusters in the sample can be identified (also observed in the photo), which is a widespread concern in solid spectroscopy and imaging of pharmaceuticals [6, 7]. The colors of the zones originate from the frequency-dependent transmission of THz light at different frequencies, as plotted in Fig. 4(c) in the main manuscript. The top-right zone of α -D-glucose monohydrate is red because it strongly absorbs in the green and blue channel, while the bottom right zone of α -D-lactose monohydrates monohydrate appears as purple due to an increased transmission in the blue and red channels. The left L-histidine hydrochloride monohydrate is the most transparent and of all and shows only a slightly pronounced absorption in the blue region.

as from the surface of the imaged object in a reflection imaging system. The results of the reflection measurement are shown in Fig. S5, however, due to the featureless THz absorption of the tablet in this frequency range, there was no hyperspectral information to be extracted and therefore the figure simply shows a cumulative intensity (grayscale) image retrieved from all beat notes in the multiheterodyne spectrum. For comparison, the right panel of the Fig. S5 shows a visible microscope photo of the tablet. Despite the small size of the sample (millimeters), and minor changes in thickness across the sample, even fine details such as the embossed letter with a submillimeter line thickness are clearly visible in the THz reflection image. Due to specular reflections from the blister packaging some interference effects are visible in the image. This effect needs to be further studied and adequately addressed if non-invasive THz pharmaceutical testing is to be implemented in this configuration. However, in principle, polymers that are opaque in the visible range, yet transparent in the THz would allow for this type of non-invasive analysis. While this example proves the compatibility of the THz-QCL OFC technology with pharmaceutical applications, to fully unlock its potential, novel gain media supporting broader comb bandwidths in THz regions with specific chemical signatures of drug constituents will have to be developed.

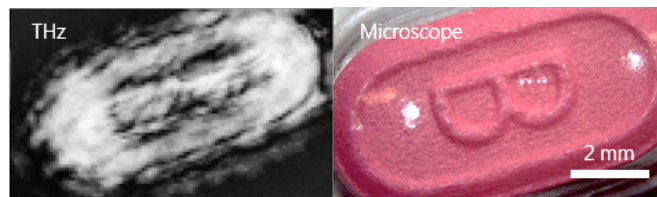


Fig. S5. THz reflection measurement. (left) of a millimeter-sized Benadryl[®] tablet in native packaging (blister) using THz-QCL OFCs together with a microscope photo (right) of the tablet.

REFERENCES

1. D. Burghoff, T.-Y. Kao, N. Han, C. W. I. Chan, X. Cai, Y. Yang, D. J. Hayton, J.-R. Gao, J. L. Reno, and Q. Hu, "Terahertz laser frequency combs," *Nat Photon* **8**, 462–467 (2014).
2. Y. Yang, D. Burghoff, D. J. Hayton, J.-R. Gao, J. L. Reno, and Q. Hu, "Terahertz multiheterodyne spectroscopy using laser frequency combs," *Optica* **3**, 499 (2016).
3. A. Hugi, G. Villares, S. Blaser, H. C. Liu, and J. Faist, "Mid-infrared frequency comb based on a quantum cascade laser," *Nature* **492**, 229–233 (2012).
4. J. Westberg, L. A. Sterczewski, and G. Wysocki, "Mid-infrared multiheterodyne spectroscopy with phase-locked quantum cascade lasers," *Appl. Phys. Lett.* **110**, 141108 (2017).
5. H. Namkung, J. Kim, H. Chung, and M. A. Arnold, "Impact of Pellet Thickness on Quantitative Terahertz Spectroscopy of Solid Samples in a Polyethylene Matrix," *Anal. Chem.* **85**, 3674–3681 (2013).
6. Y. C. Shen, T. Lo, P. F. Taday, B. E. Cole, W. R. Tribe, and M. C. Kemp, "Detection and identification of explosives using terahertz pulsed spectroscopic imaging," *Appl. Phys. Lett.* **86**, 241116 (2005).
7. J. A. Zeitler, P. F. Taday, D. A. Newnham, M. Pepper, K. C. Gordon, and T. Rades, "Terahertz pulsed spectroscopy and imaging in the pharmaceutical setting - a review," *J. Pharm. Pharmacol.* **59**, 209–223 (2007).